

Interfacial engineering of oxygenated chemical bath–deposited CdS window layer for highly efficient Sb₂Se₃ thin-film solar cells

L. Guo^{a,1}, B. Zhang^{b,1}, S. Li^c, A. Montgomery^a, L. Li^a, G. Xing^d, Q. Zhang^{c,*}, X. Qian^{b,**}, F. Yan^{a,e,***}

^a Department of Metallurgical and Materials Engineering, The University of Alabama, Tuscaloosa, AL, 35487, USA

^b Department of Materials Science and Engineering, College of Engineering and College of Science, Texas A&M University, College Station, TX, 77843, USA

^c Department of Materials Science and Engineering, Harbin University of Technology, Shenzhen, 518055, China

^d Key Laboratory of Microelectronic Devices & Integrated Technology, Institute of Microelectronics, Chinese Academy of Sciences, Beijing, 100029, China

^e Alabama Water Institute, The University of Alabama, Tuscaloosa, AL, 35487, USA

ARTICLE INFO

Article history:

Received 4 May 2019

Received in revised form

15 June 2019

Accepted 15 June 2019

Available online 28 June 2019

Keywords:

Antimony selenide

Solar cell

Close space sublimation

Oxygenated Cadmium Sulfide

Quasi-one-dimensional nanoribbons

ABSTRACT

Antimony chalcogenides with quasi-one-dimensional nanoribbon structures represent a new group of cost-effective, non-toxic, and earth-abundant materials for photovoltaics. In this work, interfacial engineering of oxygenated chemical bath–deposited (CBD) CdS buffer layers were used to tailor Sb₂Se₃ thin-film solar cells using close space sublimation (CSS) deposition process. Sb₂Se₃ solar cells with oxygenated CBD CdS have demonstrated a champion power conversion efficiency of 6.3% with graphite as back contact. Van der Waals (vdW) gap in Sb₂Se₃ is regulated via oxygen diffusion, which significantly influences the growth direction of (Sb₄Se₆)_n quasi-one-dimensional nanoribbons. The improved interface quality and ribbon orientation, in turn, enhance the electrical and optical properties as well as device performance of the Sb₂Se₃ solar cells. The defect level and corresponding device performance associated with the oxygen environment were investigated by both theoretical and experimental approaches. This work provides an effective way to tune the microstructure and electronic structure of non-cubic chalcogenides by tailoring the interfacial area between the window layer and Sb₂Se₃ absorber.

© 2019 Elsevier Ltd. All rights reserved.

1. Introduction

Solar cells, directly converting solar energy into electricity, provide renewable, sustainable, and affordable energy [1–3]. Antimony selenide, Sb₂Se₃, is considered as a promising absorber material for solar cells because of its suitable bandgap (~1.2 eV direct bandgap and 1.1 eV indirect bandgap), high absorption coefficient (~10⁵ cm^{−1}), abundant natural source as well as low toxicity compared with conventional CdTe and GaAs [4–6]. To date, the Sb₂Se₃ solar cells have been widely investigated using several grown techniques, such as CBD, rapid thermal evaporation, vapor transport deposition, and CSS, yielding the highest power

conversion efficiency (PCE) around ~9%, although the PCE is still low compared with record CdTe and CuInGaSe solar cells with PCE of ~22% [6–13]. To improve the PCE of Sb₂Se₃ solar cells, considerable strategies have been explored, including tuning the (Sb₄Se₆)_n ribbons orientation with buffer layer structure for Sb₂Se₃, such as CdS, ZnO, TiO₂ [5,6,14,15]. Selenium compensation (i.e., selenization) into the as-deposited Sb₂Se₃ suppresses the Se vacancies and improves the device performance [16]. Although CdS is toxic, it is the most commonly used window layer in CdTe solar cell because of its desired bandgap (~2.4 eV), small lattice mismatch, and *n*-type electronic behavior for the large-scale manufacturing. However, the CdS with a bandgap of 2.4 eV will absorb the blue light (photon energy > 2.4 eV) and limit the photocurrent in the solar cells [17,18]. To address this problem, reducing the CdS thickness is an effective approach to improve the light transmittance in the CdS window layer [19]. Nevertheless, thinner buffer layers may degrade open circuit voltage and fill factor because of increased pinhole concentration [20,21].

* Corresponding author.

** Corresponding author.

*** Corresponding author. Department of Metallurgical and Materials Engineering, The University of Alabama, Tuscaloosa, AL, 35487, USA.

E-mail addresses: zhangqf@hit.edu.cn (Q. Zhang), feng@tamu.edu (X. Qian), fyang@eng.ua.edu (F. Yan).

¹ These authors contributed equally.

For the Sb_2Se_3 solar cells with a CdS buffer layer, the Cd diffusion could decrease the p -type conductivity of Sb_2Se_3 because the Cd^{2+} ions occupy the Sb^{3+} site [22]. On the other hand, a small bandgap window layer can effectively improve the photocurrent by varying the device spectral response [23,24]. For example, CdSe as a window layer for CdTe could improve the photocurrent because the reduced absorber bandgap can absorb more light because of interdiffusion between CdTe and CdSe although CdSe is intrinsically a worse window layer for CdTe [24]. Postannealing of CBD CdS layer in the air can also reduce the bandgap of the CdS layer because of the recrystallization, sulfur evaporation, and self-oxidation of the CdS films [25]. In addition, oxygen in the ZnO and ambient CdCl_2 -treated CdS buffer layers for Sb_2Se_3 solar cells could significantly impact the device performance by tuning the oxygen concentration in the buffer layer, and even the oxygen introduced into the Sb_2Se_3 during film deposition could improve the efficiency due to passivation of interfacial defect states between CdS/ Sb_2Se_3 [26]. These oxygen-associated observations indicate that the oxygen in the buffer layer and absorbers plays a critical role in the Sb_2Se_3 device performance. However, it is still not clear how oxygen impacts on the Sb_2Se_3 device performance fundamentally. Particularly, how oxygen existing at the atomistic level contributes to the PCE needs to be further investigated.

In this work, we utilize the first-principles theoretical calculations to elucidate the role of oxygen in the interface between the CdS buffer layer and Sb_2Se_3 absorber layer and succeed experimentally in improving the device performance with the theoretical prediction. The oxygen-associated defects and intrinsic defects, the microstructure variation, electronic behaviors, and oxygen diffusion mechanism in Sb_2Se_3 have been systematically studied. It is demonstrated that oxygen associated defects in Sb_2Se_3 are benign defects. In addition, the enhanced device performance of Sb_2Se_3 thin-film solar cells with oxygenated CdS buffer layer can be associated with the isotropic oxygen diffusion into the Sb_2Se_3 to form an Sb–O–Se chain and fill the van der Waals (vdW) gap between the quasi-one-dimensional ribbons. We experimentally demonstrate that oxygenated CBD CdS could improve the photocurrent and open circuit voltage and boost the PCE of Sb_2Se_3 to 6.3%. The improved interfacial quality and oxygen diffusion between oxygenated CBD CdS:O buffers and Sb_2Se_3 absorber can benefit the solar cell device performance. In addition, the oxygen diffusion from the oxygenated CBD CdS could tailor the $(\text{Sb}_4\text{Se}_6)_n$ ribbon orientation. This provides a unique pathway to engineer the ribbon orientation-dependent electronic and photonic behavior and reduce heterojunction interface recombination in Sb_2Se_3 -like non-cubic chalcogenide photovoltaics.

2. Experimental details

2.1. First-principles calculations

Atomistic and electronic structures, and defect formation energy were calculated using first-principles density functional theory (DFT) [27] as implemented in the Vienna Ab initio Simulation Package (VASP) [28]. The Perdew–Burke–Ernzerhof [29] form of exchange–correlation functional within the generalized gradient approximation (GGA) [30] and a plane wave basis set with a 400 eV energy cutoff were used in the calculations. Because vdW interaction is present between neighboring $(\text{Sb}_4\text{Se}_6)_n$ ribbons, we adopted optB86–vdW non-local correlation functional that approximately accounts for dispersion interactions [31]. The structural optimization and electronic relaxation were calculated using a Γ -centered Monkhorst-Pack [32] k-point sampling grid of $4 \times 4 \times 12$. The maximal residual force of each atom was less than $0.02 \text{ eV } \text{\AA}^{-1}$ and the convergence criteria for electronic relaxation was set to

10^{-6} eV . As the DFT–GGA often underestimates the band gap, we adopt the modified Becke–Johnson (MBJ) exchange potential [33] and hybrid HSE06 functional [34] for electronic structure and optical property calculations, and a k-point grid of $12 \times 12 \times 28$ used in the MBJ calculations, and a k-point grid of $3 \times 3 \times 9$ used in the HSE06 calculations. The MBJ calculation yields a band gap close to that from the HSE06 calculation for Sb_2Se_3 . The details of charged defect formation energy and the chemical potential calculations can be found in the supporting information.

2.2. Materials and solar cells fabrication

CdS films (~60–80 nm thickness) were fabricated through chemical bath deposition on the F-doped SnO_2 -coated soda lime glass (FTO, Pilkington NSG TEC 15). FTO substrates were cleaned with Hellmanex 2% solution, acetone, isopropyl alcohol, and deionized water in an ultrasonic bath. CdSO_4 and thiourea solution were used as raw materials to form reaction solutions with NH_4OH to tune the PH value. The whole reaction took place in a chemical bath with a constant temperature of 70°C for about 10 min. Then, the CdS-coated FTOs were taken out and cleaned in deionized water to remove the loose particles. The as-deposited CdS films were annealed under various oxygen conditions in a rapid thermal process with oxygen partial pressure control. The ratio of $\text{O}_2/\text{O}_2+\text{Ar}$ was tuned to be 0%, 21%, 62%, and 92% by turning the mixture gas flows connected to argon and oxygen gas. All annealing processes were under a temperature of 400°C for 10 min. Sb_2Se_3 films were grown by CSS with pure Sb_2Se_3 powders (99.999%, Alfa Aesar) as reported previously [35]. The CdS:O-doped substrate-source distance was about 8 mm. The substrate temperature was set at 300°C , and the source temperature was 550°C . The base pressure was about 5 mTorr with Ar gas purge before the deposition. The deposited Sb_2Se_3 film was about 800 nm in thickness. Sb_2Se_3 thin-film solar cells were fabricated in conventional superstrate device structure: glass/FTO/CdS:O/ Sb_2Se_3 /Graphite/Ag. Graphite back contact was screen-printed followed by Ag slurry. Each device had a total area of approximately 0.08 cm^2 defined by the mask pattern.

2.3. Materials and solar cells characterization

The structure of CdS:O and Sb_2Se_3 film was characterized by X-ray diffraction (XRD) with $\text{Cu K}\alpha$ radiation (X'Pert). Raman experiments were conducted on a single stage Raman spectrometer with a solid-state laser (532-nm wavelength; Horiba LabRam HR). Morphology of CdS:O was investigated by atomic force microscopy (AFM, Park XE70). The absorbance and transmittance spectra were measured using a UV-Vis spectrometer (Shimadzu UV-1800). X-Ray photoelectron spectroscopy (XPS) was collected using the Kratos Axis 165 XPS with Al source. The thickness and the elemental distribution were characterized using the scanning electron microscopy (SEM, JEOL 7000) equipped with energy dispersive X-ray spectroscopy (EDS). Current density–voltage (J - V) characteristics were measured by the Newport Sol3A class AAA solar simulator (Oriel, model 94023A; Newport Corporation, Irvine, CA, USA) under ambient conditions (room temperature, 1000 W/m^2 , air mass 1.5-G illumination). A Keithley 2420 source meter (Keithley Instrument Inc.) was used to acquire J - V characteristics. External quantum efficiency (EQE) of solar cells was measured using a solar cell spectral response measurement system (QE-T, Enli Technology, Co. Ltd).

3. Results and discussion

To understand the effect of oxygen doping on Sb_2Se_3 device performance, we conduct first-principles density functional theory (DFT) calculations [27,36] and investigate the oxygen-associated

fundamental structural and electronic properties. To mimic the dilute limit of impurities, we used a $1 \times 1 \times 3$ supercell of Sb_2Se_3 . After relaxing a series of structures wherein the oxygen atom stays in a variety of potential interstitial sites, oxygen atoms can be stabilized by either locating at vdW gaps (Fig. 1a) or bonding with Sb and Se atoms within the same ribbon (i.e., forming the Sb–O–Se chain, shown in Fig. 1b). The defect tolerance of solar cell absorbers is of great importance to the device performance, where the Se rich and Se poor conditions could be used to tailor the defects and optimized the carrier transport behavior [37]. The intrinsic defect formation energy can be tuned by chemical potentials of host cell elements, while the formation energy of oxygen-induced point defects (i.e. O_i , interstitial defect) is also dependent on the chemical potential of O. Fig. 1c shows that the region of oxygen chemical potential where the formation of antimony oxides is forbidden. Chemical potentials of each element are associated with synthesis conditions. It is noteworthy that O substitution (O_{Se}) defect requires relatively low energy, indicating the possibility of oxygen occupying Se vacancy site after doping. However, Se vacancy will introduce defect localized state (DLS) as shown in Fig. 1d, which acts as carrier recombination centers. Fig. 1d also shows that oxygen interstitials are benign defects and will not introduce any mid-gap state (MGS). On the other hand, the doped O atoms may saturate at Se vacancy sites, eliminating the DLS caused by the absence of Se atoms. Our band structure calculations further confirm the transition level diagram where a flat band appears in the middle of the band gap in the host cell with Se vacancy. After adding one oxygen to Se site (i.e., O_{Se} , substitution defects), the band gap becomes clean. In addition, the band structures of the crystal with O interstitials shown in Fig. S1 do not possess any bands within the band gap, indicating the absence of DLSs. Thus, our DFT-based defect study suggests that oxygen-associated defects

in the Sb_2Se_3 absorber will not degrade the solar cell device and may even benefit the performance of Sb_2Se_3 absorber layer.

To verify our calculation results, we first systematically investigated the influences of the oxygen concentration in the CBD grown CdS thin film (~60 nm thickness) by tuning the annealing oxygen concentration to gradually introduce oxygen to the following Sb_2Se_3 through interface diffusion. The optical response was characterized using UV-Vis spectra, as shown in Fig. 2. The CdS films were annealed in 21%, 62%, and 92% oxygen partial pressure, i.e., $\text{O}_2/(\text{O}_2+\text{Ar})$ at 400 °C for 10 min. The absorbances of the oxygenated CBD CdS films are shown in Fig. 2a, where oxygenated CdS shows higher absorption in the blue range (<500 nm, red-shift in absorption edge). Meanwhile, the color of these films changes from yellow to brownish yellow, as shown in the inset of Fig. 2a, suggesting that the reduced bandgap of CdS film oxidation occurs in the presence of oxygen [25]. This is opposite to the sputtered CdS in oxygen partial pressure with increased bandgap due to wide bandgap CdSO_x formation [20]. The bandgap of these oxygenated CdS was determined as shown in Fig. 2b, where the bandgap of the films changes from 2.4 eV to 2.3 eV. When the oxygen partial pressure is less than 21%, the bandgap reduces from 2.4 to 2.31 eV because of the oxygen incorporation and CdO_x ($x=3,4$) formation with a bandgap of ~1.6 eV [38]. When increasing oxygen partial pressure more than 21%, the bandgap increases slightly, potentially because of a mixture of CdS, CdSO_3 and CdSO_4 [20,39], as shown in Fig. S2 (see in the supporting information).

The structural properties of these oxygenated CBD CdS films were characterized using the XRD (Fig. 2c). The hexagonal wurtzite structures are indexed in the figure. The XRD indicates that the crystallization is improved by introducing more oxygen. In particular, the as-deposited film annealed at lower oxygen partial pressure (<21%) displays weak intensity, while peak intensity increases

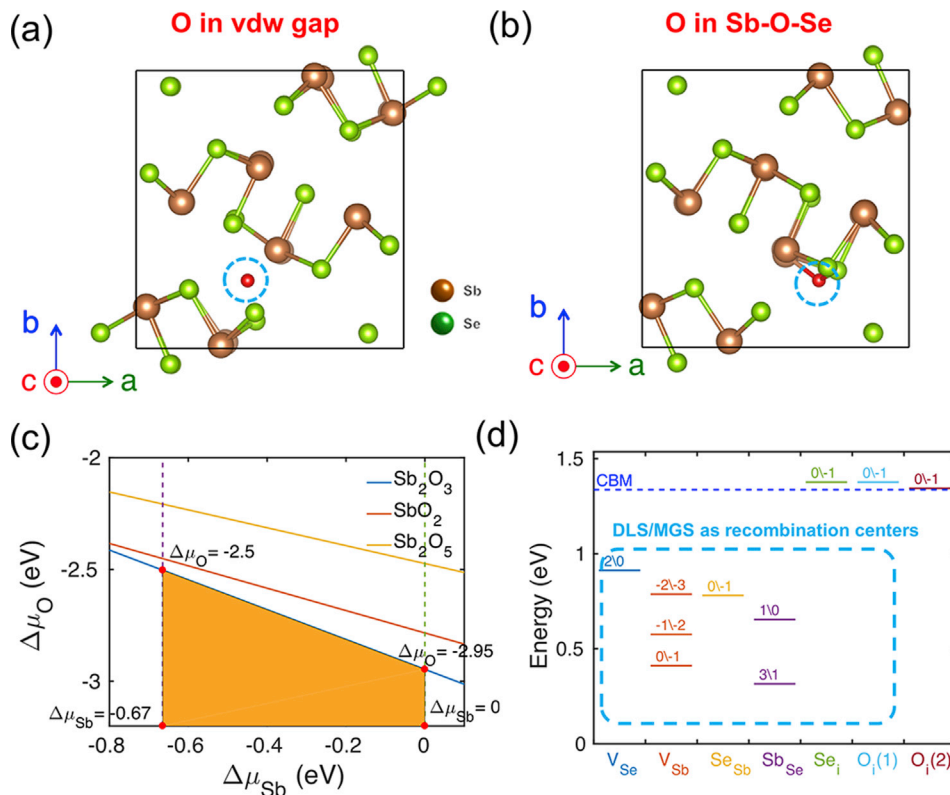


Fig. 1. (a) and (b) Two possible $\text{Sb}_2\text{Se}_3\text{:O}$ configurations: (a) O in the vdW gap and (b) Sb–O–Se chain formation. (c) The allowed chemical potential of species. (d) Charged defect transition levels. DLS: defect localized state. MGS: mid-gap state.

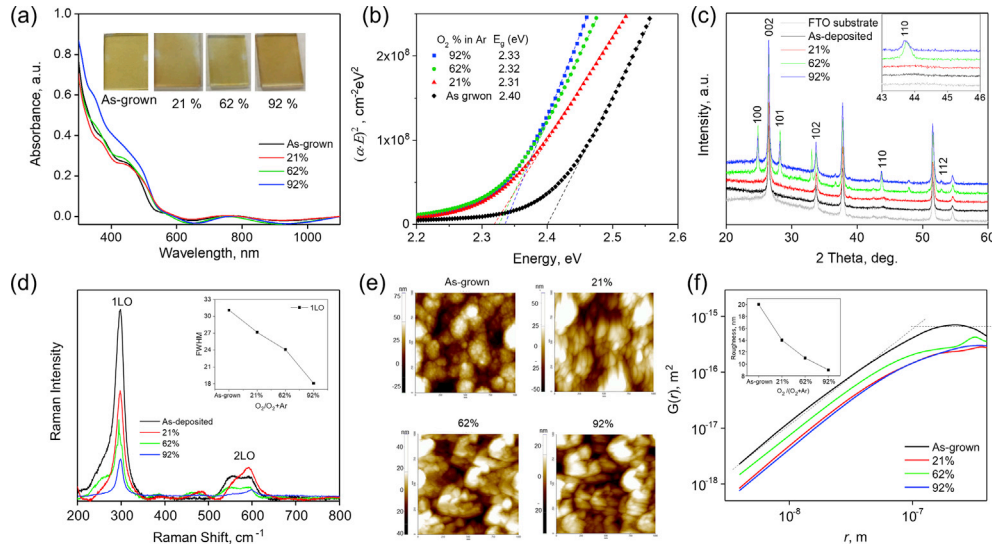


Fig. 2. Characterization of the oxygenated CBD CdS thin films treated under various oxygen partial pressures: (a) absorbance with inset of optical images of the treated films, (b) bandgap determined by the Tauc plots, (c) X-ray spectra, (d) Raman spectra, (e) atomic force microscopy (AFM) images, and (f) height profiles of the AFM images, $1 \times 1 \mu\text{m}^2$.

with increasing oxygen partial pressure, suggesting that the as-grown film exhibits nanocrystalline behavior and higher oxygen concentration improves crystallinity. In addition, the peaks at high angle (i.e. (110) peak shown in the inset of Fig. 2a) shift toward low angle at higher oxygen content, indicating slightly enlarged lattice constants of oxygenated CdS films caused by potential oxygen interstitials. Raman spectra were collected for these oxygenated CBD CdS, as shown in Fig. 2d. The longitudinal optical (LO) phonon (crystal mode) in the oxygenated CBD CdS was analyzed. The Raman intensities decrease with increased oxygen partial pressure, and the asymmetric broadening to the lower frequency can be associated with the phonon confinement effect due to the structure fluctuation [40]. However, the spectra width measured by the full width at half maximum, as shown in the inset of Fig. 2b, decreases compared to the as-grown one. It could be ascribed to that the surface oxygen on the CBD CdS [25]. Thus, the decreased bandgap (red-shift) could be directly linked to the lattice dilatation due to the interstitial oxygen with bond stretching between Cd–S (CdS:O). With the introduction of more oxygen into CdS, the slightly increased bandgap (blueshift) could be explained as the formation of CdSO_x (at higher phonon frequency, 2 LO).

To estimate the surface quality of the oxygenated CBD CdS films, AFM was used to characterize the morphology of the CdS films. Fig. 2e shows the AFM topography of CdS films oxygenated at various oxygen partial pressures. The typical polycrystalline thin films have been observed under different oxygen partial pressure. The root-mean-square roughness is significantly reduced, as shown in the inset of Fig. 2e, suggesting that the smoothening of CdS thin film is effective with the introduction of more oxygen into the CdS surface. The growth dynamics assessed from the height-height correlation function $G(r)$ is defined as $G(r) = [\langle h(\vec{r}_2) \rangle - \langle h(\vec{r}_1) \rangle]$ for each film, as shown in Fig. 2f. The curves are downshifted as oxygen partial pressure increases. It suggests that the smoothening of the oxygenated CdS could result from the oxygen on the surface diffusion toward the regions with lower surface energy (e.g., boundaries) at nanoscale [41,42]. This also indicates that the CdS:O/ Sb_2Se_3 interface quality can be improved, which may benefit the electronic and optical properties of the solar cells.

The 800-nm thick Sb_2Se_3 films were grown on the oxygenated CBD CdS:O substrates using the CSS [43]. The XRD spectra of the Sb_2Se_3 films (Fig. 3a) show high crystallinity. The observed XRD spectra agree well with the PDF-015-0861 with orthorhombic

space group (Pnma, No. 62). The calculated texture coefficients (TCs) of diffraction peaks of the samples are shown in Fig. 3b, where a large TC value suggests a preferred orientation of the grains in the films [5]. It shows that the oxygen in CdS could significantly impact the Sb_2Se_3 orientation, for example, the $\text{TC}_{(120)}$ is reduced with increasing oxygen concentration, whereas the $\text{TC}_{(211)}$ and $\text{TC}_{(221)}$ are gradually enhanced with increasing oxygen concentration. The preferred (211) and (221) orientations with the increased oxygen concentration in CdS:O suggest that the orientation of $(\text{Sb}_4\text{Se}_6)_n$ ribbon could be tuned via the oxygen diffusion from the buffer layer to the absorber. To investigate the impact of oxygenated CdS window layer on the growth behavior of the Sb_2Se_3 film, the selected (120), (211), and (221) peaks are zoomed in and shown in Fig. 3c; lattice expansion can be observed with the peak position shifted to the lower angle side when oxygen concentration increases. The calculated lattice parameters with the orthorhombic structure are shown in Fig. 3d. The a -axis lattice parameter increases from 11.4 to 11.8 Å (~2% increase) with increasing oxygen concentration in the CBD CdS buffer layer, whereas the b and c lattice parameters remain almost constant (less than 0.5% variation). This indicates the oxygen diffuses from the oxygenated CdS to Sb_2Se_3 and the a -axis expands while c axis decreases slightly. The distribution of oxygen atoms in Sb_2Se_3 may be dominated by the interstitial sites instead of substitutional oxygen on the Se sites. Otherwise, the substitution of oxygen on the Se sites should reduce the lattice parameters because of the smaller oxygen ion radius. In the case of the oxygen interstitials in Sb_2Se_3 , the possible site is the vdW gap between the $(\text{Sb}_4\text{Se}_6)_n$ ribbons in the [100] and [010] directions without dangling bonds [6]. This suggests that the oxygen in the vdW gap prefers the interstitial site that bonds to Sb/Se because the inter-chain between Se–Sb is weak [44]. The oxygen bond may be associated with the bridged ring with the stoichiometry SbSeO_x , as shown in the inset of Fig. 3e. The closed ring with –Sb–O–Se– chain could significantly impact the bond energy and bond length because of the introduced chemical strain. The Raman spectra with the oxygenated CdS window layers were shown in Fig. 3e. The Sb–O bonds (i.e., 291 cm^{-1}) appear in the Sb_2Se_3 film with oxygenated CdS window layers compared with the as-grown CdS window layer. In addition, it is notable that a new mode located at $\sim 140 \text{ cm}^{-1}$ appears in Sb_2Se_3 deposited on the oxygenated CdS window layers. This is in agreement with the Raman D1 mode at 3.6 GPa reported in high-pressure Raman scattering study on Sb_2Se_3

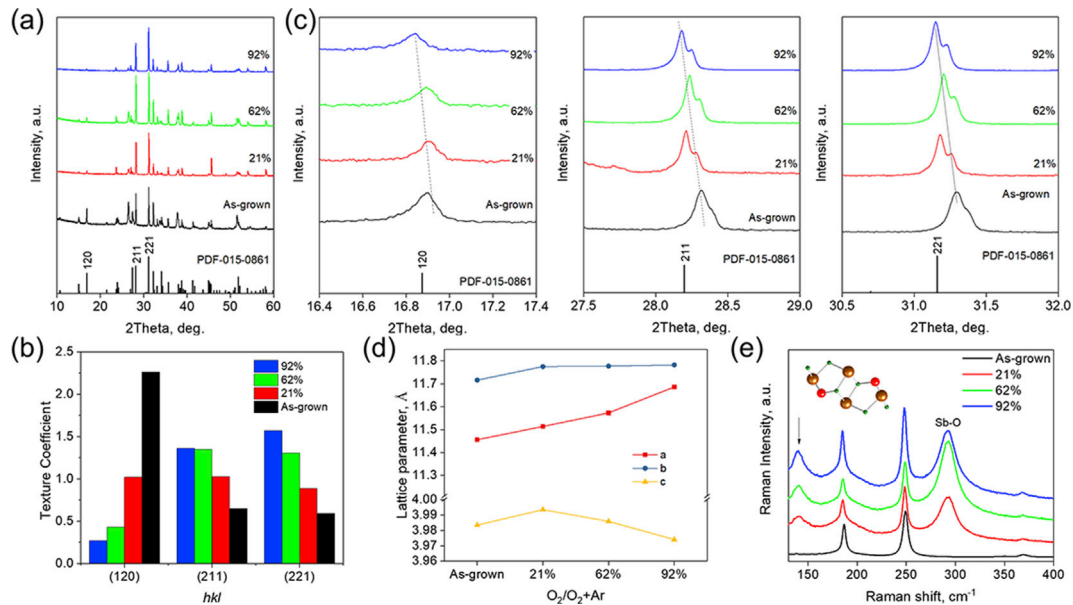


Fig. 3. Characterization of Sb₂Se₃ films grown on the oxygenated CBD CdS buffer layer. (a) X-ray diffraction (XRD) spectra of the Sb₂Se₃ films. (b) The texture coefficient for the selected peaks, (c) XRD spectra shift to lower angle in (120), (211), and (221) peaks, (d) the lattice parameters for the Sb₂Se₃, and (e) Raman spectra of the Sb₂Se₃ film. The inset of (e) shows oxygen form the bond between Sb and Se to generate the –Sb–O–Se–chain.

[45]. Meanwhile, the large lattice mismatch between the wurtzite CdS and orthorhombic Sb₂Se₃ could be reduced with Sb–O–Se bridging at the CdS/O/Sb₂Se₃ interface, which may suppress the carrier recombination at the heterojunction interface. The distribution of oxygen in the Sb₂Se₃ vdW gap could also boost the carrier transport because the (Sb₄Se₆)_n ribbons are tuned to the preferred direction, that is, normal to the substrate [6] (as shown in Fig. 3b). These observations are also in agreement with our theoretical calculation above.

To understand the oxygen distribution in the interfacial area, SEM cross-sectional analysis and corresponding EDS elemental mapping was conducted, as shown in Fig. 4. The elemental distribution of Sb and Se are uniform and in a desired 2:3 ratio, and Cd/S ratios are about 1, indicating that the Sb₂Se₃/CdS heterostructure is formed. However, the oxygen distribution (here, the oxygen from the FTO also collected) increased in the oxygenated CdS/O/Sb₂Se₃ (Fig. 4b) compared to that of CdS/Sb₂Se₃ (Fig. 4a). The oxygen in the CdS/O/Sb₂Se₃ interface can also diffuse into the Sb₂Se₃ absorber layer.

To investigate the oxygen sites in the Sb₂Se₃ absorber with CdS/O window layer, XPS was used to determine the bonding states. To prevent the surface oxygen impact, we carry out Ar ion

etching for the 20-nm top layer of the Sb₂Se₃ before measuring the XPS. As shown in Fig. 5a, the Sb 3D peaks can be observed in the as-grown Sb₂Se₃ films with as-grown CdS window layer, corresponding to the Sb 3d_{3/2}, and 3d_{5/2}, respectively. However, with the oxygenated CBD CdS/O buffer layer, two pairs of Sb 3d peaks were found with strong and weak peaks associated with Sb–Se and Sb–O bond, respectively, indicating oxygen diffuses from the oxygenated CdS buffer layer into the Sb₂Se₃ absorber layer. Meanwhile, Fig. 4b and d show the Se 3D spectra with CdS and CdS/O buffer layer, respectively. It demonstrates that the Se–O bond is formed in the oxygenated CdS buffer layer (Fig. 5d), suggesting that the oxygen diffused from the CdS/O layer also form bonds with the Se ions. It may form Sb–O–Se chains or SbSeO_x compounds in Sb₂Se₃ film, consistent with the tentatively proposed crystal structures by first-principles calculations in Fig. 1a and b.

Fig. 5a illustrates the cell structure with the oxygenated CBD CdS buffer layer and the graphite top electrode. As shown in Fig. 6b, the band alignment among CdS, oxygenated CdS/O, and Sb₂Se₃ leads to the electron-hole pair dissociation and charge transfer at the interface. With the introduction of oxygen at the interface of CdS/Sb₂Se₃ and the oxygen-filled vdW gap in Sb₂Se₃, the heterostructure interface quality is improved and graded bandgap may be

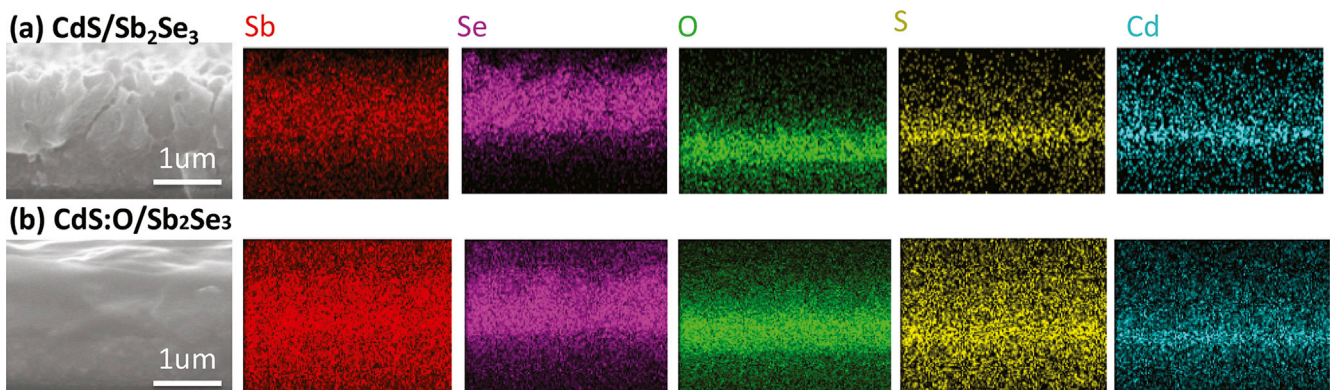


Fig. 4. Cross-sectional SEM and EDS elemental mapping for (a) CdS/Sb₂Se₃ and (b) 91% O/Ar + O annealed CdS/O/Sb₂Se₃ thin film. SEM, scanning electron microscopy.

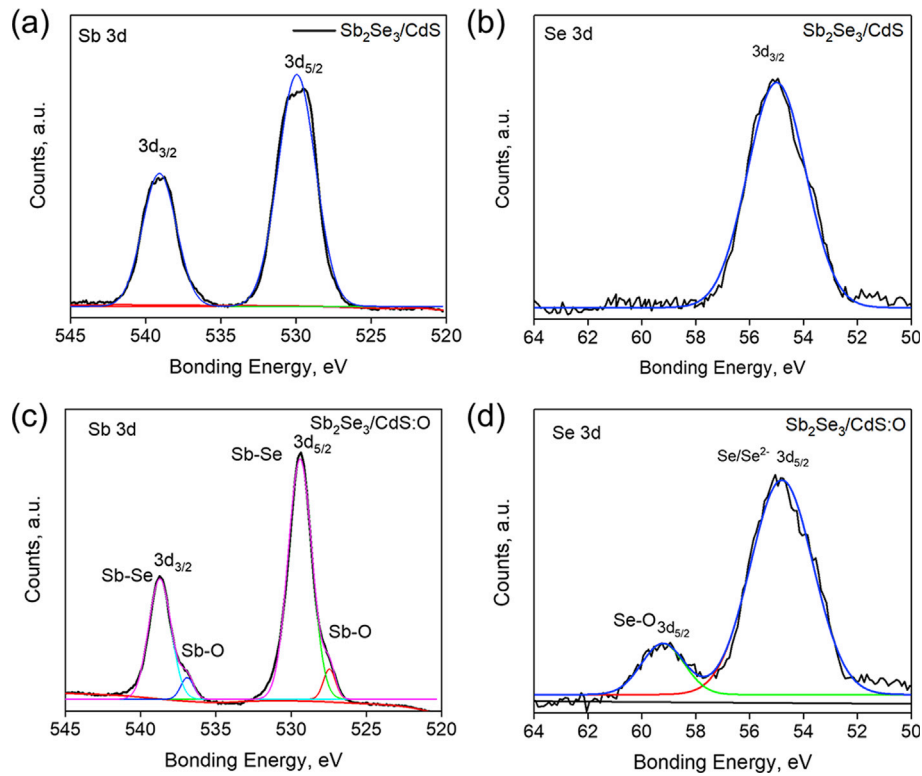


Fig. 5. XPS of Sb_2Se_3 film with oxygenated CBD CdS. Sb 3d with (a) CdS and (c) CdS:O buffer layer and XPS of Se 3d with (b) CdS and (d) CdS:O buffer layer. XPS, X-ray photoelectron spectroscopy.

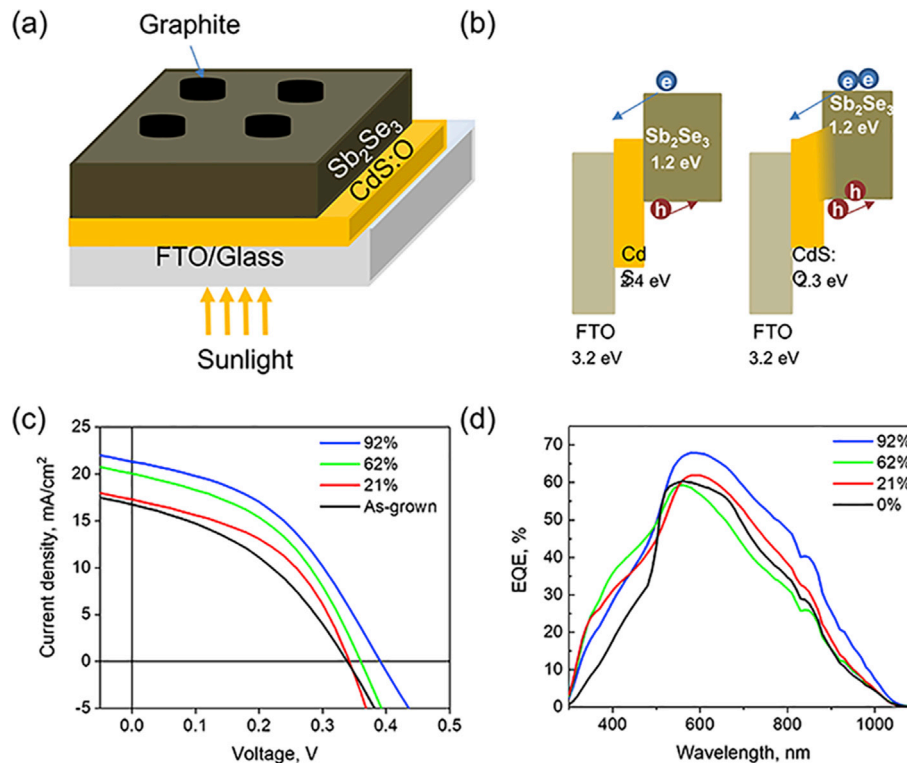


Fig. 6. Sb_2Se_3 solar cell device performance with the oxygenated CdS buffer layer. (a) Current density-voltage (J - V) curves and (b) external quantum efficiency (EQE) spectra of the Sb_2Se_3 solar cells on oxygenated CdS films.

Table 1
Device parameters of glass/TCO/CdS:O/Sb₂Se₃/graphite solar cell devices.

O ₂ % in CdS:O	V _{oc} , V	J _{sc} , mA/cm ²	Fill factor, FF, %	PCE, %	R _s , Ω cm ²	R _{sh} , Ω cm ²
As-grown	0.338	16.71	39.3	2.2	114.8	799.8
21%	0.341	17.28	45.9	2.70	73.6	946.5
62%	0.360	20.01	44.3	3.19	83.8	889.8
92%	0.391	21.32	43.1	3.59	108.1	1016.1

PCE, power conversion efficiency.

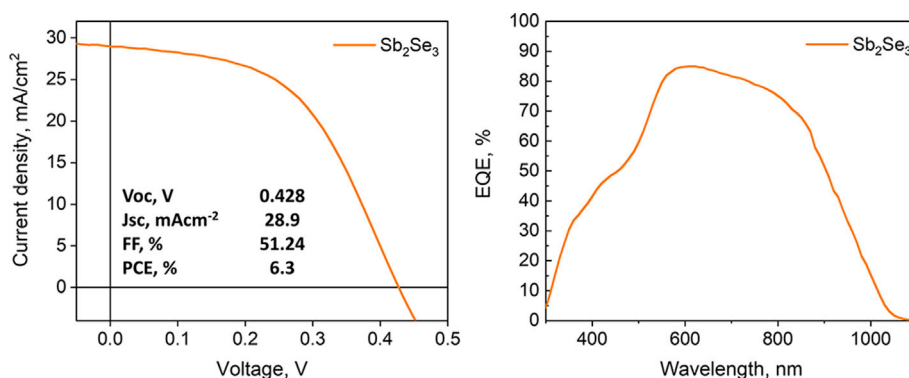


Fig. 7. Sb₂Se₃ solar cell champion device with the optimized oxygenated CdS buffer layer. (a) Current density-voltage (*J*–*V*) curves and (b) external quantum efficiency (EQE) spectra of the Sb₂Se₃ solar cells on oxygenated CBD CdS films.

formed due to the consumption of oxygen. The oxygen inside the Sb₂Se₃ vdW gaps may assist carrier transport across the gap. Thus, better device performance is expected in the oxygenated CdS buffer layer. Fig. 6c shows the *J*–*V* curves of typical Sb₂Se₃ solar cells in the configuration FTO/CdS:O/Sb₂Se₃/graphite/Ag. The corresponding device parameters are given in Table 1. The oxygenated CdS in 92% oxygen partial pressure achieved the best device performance as expected with PCE of 3.59%, V_{oc} of ~0.391 V, and J_{sc} of 21.32 mA cm⁻². Here, the improved V_{oc} and J_{sc} could be attributed to the tilted (Sb₄Se₆)_n ribbons normal to the substrate (as proved previously through the texture coefficient analysis) and the suppressed interface recombination. The series resistivity (R_{oc}) and shunt resistivity (R_{sh}) show slight improvement with increasing oxygen concentration, in good agreement with other oxygenated CdS-buffered solar cells because of the improved resistivity of oxygenated CdS layer [20]. Another potential reason for the improved resistivity may be ascribed to the Sb₂Se₃ absorber layer with more oxygen [14]. As shown in Fig. 6d, the EQE curves of these CdS:O/Sb₂Se₃ cells demonstrate an enhanced photoabsorption in the short (<500 nm) and long (>700) wavelength regions, indicating the improved current collection in these two regions. In addition, the EQE maxima shift from ~2.3 to ~2.1 eV with increasing oxygen partial pressure, confirming a redshift associated with the decreased bandgap of CdS:O buffer layers, which is in agreement with our previous UV-Vis optical measurement.

With the optimization of the oxygenated CBD CdS window layer thickness (~80 nm), Sb₂Se₃ CSS growth condition and thickness (e.g., tuning the growth rate), and reduced graphite electrode resistivity, we achieved a champion solar cell with V_{oc} of 0.428 V, J_{sc} of 28.9 mAcm⁻² and fill factor (*FF*) of 51.24% and a PCE of 6.3% (as shown in Fig. 7a). The device optimization process can be found elsewhere [43]. This is among the highest efficiencies so far for Sb₂Se₃ solar cells with graphite back contact. Here, the low *FF* compared with the reported high-efficiency Sb₂Se₃ solar cells may be ascribed to the higher series resistivity of the graphite electrode and interface between Sb₂Se₃/graphite compared to the cells with thin Au electrode [5,11]. The EQE response for the champion devices was shown in Fig. 7b. An EQE of 85% can be achieved at a

wavelength of 604 nm, which is on a par with the previously reported high-efficiency Sb₂Se₃ devices, slightly lower because of the lack of the hole transport layer, such as PbS, spiro-OMeTAD [4,12].

4. Conclusion

In summary, the interface engineering of oxygenated CBD CdS buffer layer has been used to tailor the Sb₂Se₃ solar cells to achieve high PCE of ~6.3%. The study of native and extrinsic defects in the absorber layer, the fundamental structural and electronic properties of Sb₂Se₃ with potential O-doped defects, the interface engineering of microstructure and electronic structure in the oxygenated CBD CdS have been systematically investigated using both theoretical and experimental methods. The Sb₂Se₃ films show gradual lattice expansion in *a*-axis direction, suggesting that oxygen diffuses from oxygenated CdS buffer layer to the interstitial sites in the vdW gap of the inter-Sb₂Se₃ nanoribbons, stabilized by the formation of Sb–O–Se chain. The (Sb₄Se₆)_n nanoribbons were also found to be normal to the substrate with increasing oxygen in the CdS:O buffer because of the preference of forming Sb–O–Se chains. Our work demonstrates that the optimized buffer/Sb₂Se₃ interface and oxygen in Sb₂Se₃ could provide a unique pathway to tailor the optical and electronic behavior and improve the efficiency of non-cubic chalcogenide solar cells.

Conflict of interest

There are no conflicts of interest.

Acknowledgments

L.G. and B.Z. contributed equally to this work. F.Y. acknowledges the support of the Alabama Water Institute at the University of Alabama. Q. Z. acknowledges the Shenzhen fundamental research projects (JCYJ2016060816100082). X.Q. acknowledges partial 8161000821 support by National Science Foundation (NSF) under award number DMR-1753054 and OAC-1835690. Portions of this

research were conducted with the advanced computing resources provided by Texas A&M High Performance Research Computing.

Appendix A. Supplementary data

Supplementary data to this article can be found online at <https://doi.org/10.1016/j.mtphys.2019.100125>.

References

- [1] A. Polman, M. Knight, E.C. Garnett, B. Ehrler, W.C. Sinke, Photovoltaic materials: present efficiencies and future challenges, *Science* 352 (6283) (2016).
- [2] S. Chu, Y. Cui, N. Liu, The path towards sustainable energy, *Nat. Mater.* 16 (2016) 16.
- [3] M.A. Green, S.P. Bremner, Energy conversion approaches and materials for high-efficiency photovoltaics, *Nat. Mater.* 16 (2016) 23.
- [4] C. Chen, L. Wang, L. Gao, D. Nam, D.B. Li, K.H. Li, Y. Zhao, C. Ge, H. Cheong, H. Liu, H.S. Song, J. Tang, 6.5% certified efficiency Sb_2Se_3 solar cells using PbS colloidal quantum dot film as hole-transporting layer, *ACS. Energy Lett.* 2 (9) (2017) 2125–2132.
- [5] L. Wang, D.B. Li, K.H. Li, C. Chen, H.X. Deng, L. Gao, Y. Zhao, F. Jiang, L.Y. Li, F. Huang, Y.S. He, H.S. Song, G.D. Niu, J. Tang, Stable 6%-efficient Sb_2Se_3 solar cells with a ZnO buffer layer, *Nat. Energy* 2 (4) (2017).
- [6] Y. Zhou, L. Wang, S. Chen, S. Qin, X. Liu, J. Chen, D.-J. Xue, M. Luo, Y. Cao, Y. Cheng, E.H. Sargent, J. Tang, Thin-film Sb_2Se_3 photovoltaics with oriented one-dimensional ribbons and benign grain boundaries, *Nat. Photon.* 9 (2015) 409.
- [7] Z. Li, X. Liang, G. Li, H. Liu, H. Zhang, J. Guo, J. Chen, K. Shen, X. San, W. Yu, R.E.I. Schropp, Y. Mai, 9.2%-efficient core-shell structured antimony selenide nanorod array solar cell, *Nat. Commun.* 10 (125) (2019).
- [8] D. Perez-Martinez, J.D. Gonzaga-Sanchez, F. De Bray-Sanchez, G. Vazquez-Garcia, J. Escorcia-Garcia, M.T.S. Nair, P.K. Nair, Simple solar cells of 3.5% efficiency with antimony sulfide-selenide thin films, *Phys. Status Solidi-R* 10 (5) (2016) 388–396.
- [9] K. Zeng, D.J. Xue, J. Tang, Antimony selenide thin-film solar cells, *Semicond. Sci. Technol.* 31 (6) (2016).
- [10] X.Z. Wu, High-efficiency polycrystalline CdTe thin-film solar cells, *Sol. Energy* 77 (6) (2004) 803–814.
- [11] C.C. Yuan, L.J. Zhang, W.F. Liu, C.F. Zhu, Rapid thermal process to fabricate Sb_2Se_3 thin film for solar cell application, *Sol. Energy* 137 (2016) 256–260.
- [12] D.B. Li, X.X. Yin, C.R. Grice, L. Guan, Z.N. Song, C.L. Wang, C. Chen, K.H. Li, A.J. Cimaroli, R.A. Awani, D.W. Zhao, H.S. Song, W.H. Tang, Y.F. Yan, J. Tang, Stable and efficient $\text{CdS}/\text{Sb}_2\text{Se}_3$ solar cells prepared by scalable close space sublimation, *Nanomater. Energy* 49 (2018) 346–353.
- [13] X. Wen, C. Chen, S. Lu, K. Li, R. Kondrotas, Y. Zhao, W. Chen, L. Gao, C. Wang, J. Zhang, G. Niu, J. Tang, Vapor transport deposition of antimony selenide thin film solar cells with 7.6% efficiency, *Nat. Commun.* 9 (1) (2018) 2179.
- [14] C. Chen, Y. Zhao, S. Lu, K. Li, Y. Li, B. Yang, W. Chen, L. Wang, D. Li, H. Deng, F. Yi, J. Tang, Accelerated optimization of $\text{TiO}_2/\text{Sb}_2\text{Se}_3$ thin film solar cells by high-throughput combinatorial approach, *Adv. Energy Mater.* 7 (20) (2017) 1700866.
- [15] X. Wen, Y. He, C. Chen, X. Liu, L. Wang, B. Yang, M. Leng, H. Song, K. Zeng, D. Li, K. Li, L. Gao, J. Tang, Magnetron sputtered ZnO buffer layer for Sb_2Se_3 thin film solar cells, *Sol. Energy Mater. Sol. Cell.* 172 (2017) 74–81.
- [16] M. Leng, M. Luo, C. Chen, S. Qin, J. Chen, J. Zhong, J. Tang, Selenization of Sb_2Se_3 absorber layer: an efficient step to improve device performance of $\text{CdS}/\text{Sb}_2\text{Se}_3$ solar cells, *Appl. Phys. Lett.* 105 (8) (2014): 083905.
- [17] J.M. Kephart, R. Geisthardt, W.S. Sampath, Sputtered, oxygenated CdS window layers for higher current in CdS/CdTe thin film solar cells, in: 2012 38th IEEE Photovoltaic Specialists Conference, 2012, pp. 000854–000858.
- [18] N.R. Paudel, C.R. Grice, C. Xiao, Y. Yan, The effects of high-temperature processing on the structural and optical properties of oxygenated CdS window layers in CdTe solar cells, *J. Appl. Phys.* 116 (4) (2014): 044506.
- [19] D.M. Meysing, C.A. Wolden, M.M. Griffith, H. Mahabadi, J. Pankow, M.O. Reese, J.M. Burst, W.L. Rance, T.M. Barnes, Properties of reactively sputtered oxygenated cadmium sulfide (CdS/O) and their impact on CdTe solar cell performance, *J. Vac. Sci. Technol. A* 33 (2) (2015).
- [20] J. Ge, P. Koirala, C.R. Grice, P.J. Roland, Y. Yu, X.X. Tan, R.J. Ellingson, R.W. Collins, Y.F. Yan, Oxygenated CdS buffer layers enabling high open-circuit voltages in earth-abundant $\text{Cu}_2\text{BaSnS}_4$ thin-film solar cells, *Adv. Energy Mater.* 7 (6) (2017).
- [21] M.M. Junda, C.R. Grice, I. Subedi, Y.F. Yan, N.J. Podraza, Effects of oxygen partial pressure, deposition temperature, and annealing on the optical response of CdS/O thin films as studied by spectroscopic ellipsometry, *J. Appl. Phys.* 120 (1) (2016).
- [22] Y. Zhou, Y. Li, J.J. Luo, D.B. Li, X.S. Liu, C. Chen, H.B. Song, J.Y. Ma, D.J. Xue, B. Yang, J. Tang, Buried homojunction in $\text{CdS}/\text{Sb}_2\text{Se}_3$ thin film photovoltaics generated by interfacial diffusion, *Appl. Phys. Lett.* 111 (1) (2017).
- [23] N.R. Paudel, Y. Yan, Enhancing the photo-currents of CdTe thin-film solar cells in both short and long wavelength regions, *Appl. Phys. Lett.* 105 (18) (2014) 183510.
- [24] J.D. Poplawsky, W. Guo, N. Paudel, A. Ng, K. More, D. Leonard, Y. Yan, Structural and compositional dependence of the $\text{CdTe}_{1-x}\text{Se}_x$ alloy layer photo-activity in CdTe-based solar cells, *Nat. Commun.* 7 (2016) 12537.
- [25] H. Metin, R. Esen, Annealing studies on CBD grown CdS thin films, *J. Cryst. Growth* 258 (1) (2003) 141–148.
- [26] L. Wang, M. Luo, S.K. Qin, X.S. Liu, J. Chen, B. Yang, M.Y. Leng, D.J. Xue, Y. Zhou, L. Gao, H.S. Song, J. Tang, Ambient CdCl_2 treatment on CdS buffer layer for improved performance of Sb_2Se_3 thin film photovoltaics, *Appl. Phys. Lett.* 107 (14) (2015).
- [27] P. Hohenberg, W. Kohn, Inhomogeneous electron gas, *Phys. Rev.* 136 (3B) (1964) B864–B871.
- [28] G. Kresse, J. Furthmüller, Efficient iterative schemes for ab initio total-energy calculations using a plane-wave basis set, *Phys. Rev. B* 54 (16) (1996) 11169–11186.
- [29] J.P. Perdew, K. Burke, M. Ernzerhof, Generalized gradient approximation made simple, *Phys. Rev. Lett.* 77 (18) (1996) 3865–3868.
- [30] D.C. Langreth, M.J. Mehl, Beyond the local-density approximation in calculations of ground-state electronic properties, *Phys. Rev. B* 28 (4) (1983) 1809–1834.
- [31] J. Klimeš, D.R. Bowler, A. Michaelides, Van der Waals density functionals applied to solids, *Phys. Rev. B* 83 (19) (2011) 195131.
- [32] H.J. Monkhorst, J.D. Pack, Special points for Brillouin-zone integrations, *Phys. Rev. B* 13 (12) (1976) 5188–5192.
- [33] A.D. Becke, E.R. Johnson, A simple effective potential for exchange, *J. Chem. Phys.* 124 (22) (2006) 221101.
- [34] A.V. Krukau, O.A. Vydrov, A.F. Izmaylov, G.E. Scuseria, Influence of the exchange screening parameter on the performance of screened hybrid functionals, *J. Chem. Phys.* 125 (22) (2006) 224106.
- [35] L. Guo, B. Zhang, Y. Qin, D. Li, L. Li, X. Qian, F. Yan, Tunable quasi-one-dimensional ribbon enhanced light absorption in Sb_2Se_3 thin-film solar cells grown by close-space sublimation, *Solar RRL* 2 (10) (2018) 1800128.
- [36] W. Kohn, L.J. Sham, Self-consistent equations including exchange and correlation effects, *Phys. Rev.* 140 (4A) (1965) A1133–A1138.
- [37] X. Liu, X. Xiao, Y. Yang, D.-J. Xue, D.-B. Li, C. Chen, S. Lu, L. Gao, Y. He, M.C. Beard, G. Wang, S. Chen, J. Tang, Enhanced Sb_2Se_3 solar cell performance through theory-guided defect control, *Prog. Photovoltaics Res. Appl.* 25 (10) (2017) 861–870.
- [38] C.Y. Moon, S.H. Wei, Y.Z. Zhu, G.D. Chen, Band-gap bowing coefficients in large size-mismatched II-VI alloys: first-principles calculations, *Phys. Rev. B* 74 (23) (2006).
- [39] D.A. Duncan, J.M. Kephart, K. Horsley, M. Blum, M. Mezher, L. Weinhardt, M. Häming, R.G. Wilks, T. Hofmann, W. Yang, M. Bär, W.S. Sampath, C. Heske, Characterization of sulfur bonding in CdS/O buffer layers for CdTe-based thin-film solar cells, *ACS Appl. Mater. Interfaces* 7 (30) (2015) 16382–16386.
- [40] P. Parayanthal, F.H. Pollak, Raman scattering in alloy semiconductors: "spatial correlation" model, *Phys. Rev. Lett.* 52 (20) (1984) 1822–1825.
- [41] T. Karabacak, Y.P. Zhao, G.C. Wang, T.M. Lu, Growth-front roughening in amorphous silicon films by sputtering, *Phys. Rev. B* 64 (8) (2001): 085323.
- [42] A. Panin, A. Shugurov, Smoothing of thin film surfaces, in: Proceedings KORUS 2000. The 4th Korea-Russia International Symposium on Science and Technology, vol. 3, 2000, pp. 209–214.
- [43] L. Guo, B. Zhang, Y. Qin, D. Li, L. Li, X. Qian, F. Yan, Tunable quasi-one-dimensional ribbon enhanced light absorption in Sb_2Se_3 thin-film solar cells grown by close-space sublimation, *Solar RRL* 0 (0) (2018) 1800128.
- [44] V.L. Deringer, R.P. Stoffel, M. Wuttig, R. Dronskowski, Vibrational properties and bonding nature of Sb_2Se_3 and their implications for chalcogenide materials, *Chem. Sci.* 6 (9) (2015) 5255–5262.
- [45] I. Efthimiopoulos, J.M. Zhang, M. Kucway, C. Park, R.C. Ewing, Y.J. Wang, Sb_2Se_3 under pressure, *Sci. Rep.* 3 (2013) 2665.